World Electric Vehicle Journal

MDPI

Article

Joint Estimation of Driving State and Road Surface Adhesion Coefficient of a Four-Wheel Independent and Steering-Drive Electric Vehicle

Zhixin Chen, Gang Li *, Zhihua Zhang and Ruolan Fan

School of Automobile and Traffic Engineering, Liaoning University of Technology, Jinzhou 121001, China; 221291012@stu.lnut.edu.cn (Z.C.); zzh159258@163.com (Z.Z.); 219922005@stu.lnut.edu.cn (R.F.)
* Correspondence: qcxyligang@lnut.edu.cn

Abstract: Vehicle running state parameters and road surface state are crucial to the stability of four-wheel independent drive and steering electric vehicle control. Therefore, this study explores the estimation of vehicle driving state parameters and road surface adhesion coefficients using a combination of federal Kalman filtering and an intelligent bionic antlion optimization algorithm. Firstly, according to the research purpose of the paper and the focus on the accuracy of the establishment of the three degrees of freedom dynamics model, fully considering the road conditions, the paper adopts the Dugoff tire model and finally completes the establishment of the vehicle state estimation model. Secondly, the drive state estimation algorithm is developed utilizing the principles of federal Kalman filtering and volume Kalman filtering. At the same time, robust estimation theory is introduced into the sub-filter, and the antlion optimization module is designed at the lower layer of the main filter to enhance the accuracy of estimates. It is easy to see that the design of the Antlion federal Kalman travel state estimation algorithm has noticeably enhanced accuracy and traceability, according to the result. Thirdly, a joint estimation algorithm of state estimation and road surface adhesion coefficient has been devised to enhance the stability and precision of the estimation process. Finally, the results showed that the joint estimation algorithm has high accuracy in estimating vehicle driving state parameters such as the center of mass lateral deflection angle and road surface adhesion coefficient by simulation.

Keywords: federal Kalman filter; antlion optimization; driving state estimation

Citation: Chen, Z.; Li, G.; Zhang, Z.; Fan, R. Joint Estimation of Driving State and Road Surface Adhesion Coefficient of a Four-Wheel Independent and Steering-Drive Electric Vehicle. *World Electr. Veh. J.* **2024**, *15*, 249. https://doi.org/10.3390/wevj15060249

Academic Editor: Peter Van den Bossche

Received: 8 May 2024
Revised: 30 May 2024
Accepted: 4 June 2024
Published: 7 June 2024

1. Introduction

The four-wheel independent drive electric vehicle (4WID-EV) represents a pivotal configuration in electric vehicle design, positioning the drive motor directly within the wheel rim and employing the rim motor as the active onboard driving force. This setup, in contrast to conventional centralized drive systems, eliminates transmission components like differentials, reducers, and half shafts. The distinctive four-wheel autonomous drive and control architecture endow the vehicle with superior mobility and adaptability. Such enhancements enable the vehicle to adeptly navigate complex and fluctuating road conditions and meet diverse driving demands, thereby optimizing the low-speed agility and high-speed stability of electric vehicles. Nonetheless, the intricate nature of this configuration presents substantial challenges for accurately estimating the vehicle's driving state and developing advanced dynamic control systems.

With the rapid development of electronic control technology, advanced electronic control systems such as adaptive cruise control, vehicle stability control, direct yaw torque control, and anti-lock braking control have been widely used in vehicles [1–4]. This not only greatly improves the driving stability and safety of the vehicle but also makes the vehicle have a certain autonomous performance. The American Society of Automotive Engineers (SAE) divides the level of automobile autonomy into 0–5 levels: level 0 is non-automatic

and completely controlled by people; level 1 is somewhat automated, but level 2 is still human-based; level 2 is semi-automatic, self-driving works in some places; level 3 mainly depends on the self-driving system but must be equipped with human drivers to deal with emergencies. Level 4 is autopilot in some specific circumstances, with no need for people; level 5 is no need for people in any environment [5]. Whether it is a vehicle of any autonomous grade, the handling and stability of the vehicle are particularly important for safety. However, the important factor affecting the handling and stability of the vehicle is the tire.

As one of the important components of the vehicle, the tire is also the only part of the vehicle in contact with the ground, and its role is very important in vehicle dynamics. However, a critical factor determining tire performance is tire pressure [6]. Therefore, tire pressure directly affects vehicle driving performance. Various studies show that tire pressure has an important influence on vehicle power, passability, ride comfort, braking, handling stability, and so on. Among them, the handling and stability of the vehicle are determined by the cornering characteristics of the tire. Cornering stiffness is an important tire parameter that determines handling and stability. When the cornering force of the tire reaches the adhesion limit, the wheel will slip. In reference [6], the test of the effect of tire pressure on vehicle cornering characteristics shows that the cornering stiffness increases with the increase of tire pressure, but the cornering stiffness no longer changes when the tire pressure is too high [6–10]. After the tire is selected, the tire pressure is not only the key factor affecting the tire cornering characteristics but also the key factor affecting the handling and stability of the vehicle [11,12].

Vehicle dynamics control strategies are based on the current driving state and the corresponding road information to implement the corresponding control logic, and the intention of the driver and the driving state parameter information such as the center of mass lateral deflection angle, longitudinal/lateral speed, the yaw angular velocity, and road surface adhesion are the necessary prerequisites for this type of control system. Among them, the yaw angular velocity represents the state of left and right rotation of the vehicle body during driving and reflects the steering performance and stability of the vehicle, and the center of mass lateral deflection angle represents the degree to which the vehicle deviates from the expected trajectory, which determines the tracking ability of the vehicle. The road surface adhesion coefficient is the ratio of tire longitudinal force to vertical force, and at the same time, the road adhesion coefficient is also the proportional coefficient between tire radial reaction force and adhesion force. On a road surface with a constant adhesion coefficient, the adhesion force is expressed as the limit value of the reverse force acting on the tire. On a fixed road surface, the tire adhesion force can be adjusted by changing the tire reaction force so that the vehicle can obtain higher driving performance. Sensors are key devices for acquiring driving state parameters, but they are subject to errors. Meanwhile, the vehicle driving conditions are very complex, and some parameters will change in real time with the different driving conditions. In addition, with the increase in vehicle control systems and driving assistance systems, the demand for precise estimation of driving state parameters in real-time is becoming higher and higher. This requires that the algorithm not only deal with complex nonlinear problems and multi-source information fusion problems but also be able to respond quickly and give accurate estimation results in time [13–16]. Therefore, how to precisely estimate the state parameters is very important in the automobile field. Based on this background, this paper conducts a joint estimation of vehicle driving state and road surface adhesion coefficient through the study of four-wheel independent drive and steering electric vehicles.

In Reference [17], a state parameter estimation algorithm founded on the vehicle dynamics model and the Kalman filter theory is used to process the collected sensor data, which can accurately estimate the vehicle speed and steering angle. In Reference [18], combining the characteristics of vehicle dynamics and fuzzy theory, a representative T-S fuzzy model was built, the influence of longitudinal speed change was considered, and the state parameters were estimated. The state parameters of a four-wheel independent drive

electric vehicle to be estimated according to the particle filter algorithm are in reference [19]. Experimental outcomes indicate that the algorithm is superior to the estimation of a nonlinear system. Reference [20] designs an estimation algorithm for vehicle state parameters based on a neural network model and uses experimental data to train the neural network model, precisely estimating vehicle speed and acceleration. Reference [21] combines the neural network model with fuzzy control theory and uses information such as longitudinal vehicle speed and steering wheel angle parameters as input for training the neural network to complete the estimation of the center of mass lateral deflection angle. The experimental findings demonstrate that this method offers high accuracy in observation. Reference [22] uses a method of multi-sensor fusion to estimate a vehicle's state parameters. Through the fusion processing of the data collected by radar and camera, an accurate estimation of the vehicle's current position and operating speed is achieved. In reference [23], we utilize the fusion processing of information provided by radar and inertial measurement units to achieve an accurate estimation of vehicle attitude and trajectory. Reference [24] designs a kind of vehicle state estimation algorithm using the federal Kalman filter theory to achieve adaptive adjustment to changes in process noise. Reference [25] designs a peak attachment coefficient observer and a center of mass lateral deflection angle state observer for joint estimation. The algorithm requires only the most basic signals as inputs and has the advantages of low cost and reliability. Chan [26] designed an EKF estimation with a double-layer structure, which reduces the impact of vehicle parameters, road surface adhesion coefficient, and slope changes on the estimation accuracy and has higher estimation accuracy and robustness to vehicle parameter changes.

This paper designs an antlion federal Kalman joint estimation algorithm based on federal Kalman filtering and intelligent bionic antlion optimization theory to perform joint estimation of vehicle state parameters and road surface adhesion coefficient.

2. Vehicle Modeling

Kinematic analysis and dynamic analysis are usually used in vehicle modeling, and different estimation methods can be used according to different modeling methods. Considering the accuracy requirements of the two kinds of models and the characteristics of estimation methods, the estimation method adopted for the dynamic model is studied in this paper.

2.1. Three Degrees of Freedom Dynamic Model

According to the purpose of this study, we mainly pay attention to the planar motion of the vehicle's characteristics and the real-time operation, simplify the complex vehicle model, ignore the roll, pitch motion, and rotation of the four wheels around the axis, and only consider the three degrees of freedom, which are longitudinal, lateral, and yaw directions, to build a nonlinear dynamic model of the vehicle, as shown in Figure 1, which can fully express the dynamic response of the vehicle system's characteristics.

The modeling is based on the following assumptions:

(1) It is assumed that the vehicle is a rigid car body, and the coordinate origin of the vehicle dynamic model coincides with the center of mass.
(2) I ignore the influence of air resistance, road friction resistance, etc.
(3) It is assumed that the mechanical properties of each tire are the same.
(4) The influence of the suspension system on the motion of the vehicle is ignored, and the degrees of freedom of the roll and pitch directions of the vehicle are ignored.

According to the analysis in Figure 1, the vehicle motion differential equations are shown below:

$$\dot{u} = a_x + vr \tag{1}$$

$$\dot{v} = a_y - ur \tag{2}$$

$$\dot{r} = \frac{1}{Iz}\Gamma \tag{3}$$

where a_x is the longitudinal acceleration, a_y is the lateral acceleration, u is the longitudinal speed, v is the lateral speed, I_z is the moment of inertia around the z axis, and Γ is the yaw moment.

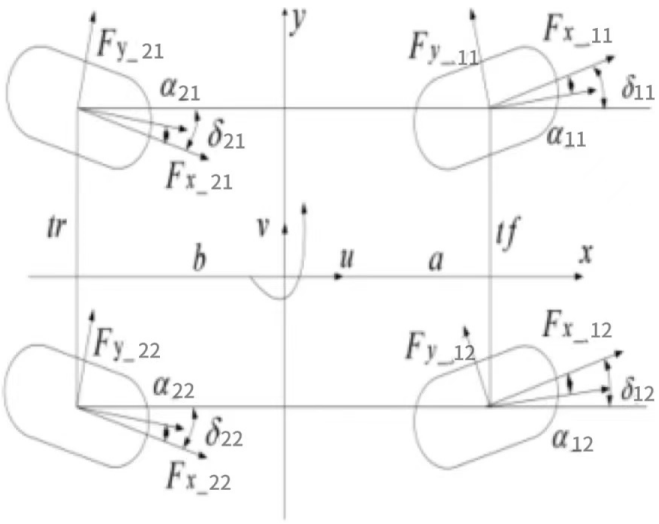

Figure 1. Vehicle dynamics model.

Perform force analysis on the vehicle dynamics model to calculate longitudinal/lateral acceleration and yaw moment, as shown below:

$$\begin{aligned} ma_x = {} & F_{x\_11}\cos\delta_{11} - F_{y\_11}\sin\delta_{11} + F_{x\_12}\cos\delta_{12} - F_{y\_12}\sin\delta_{12} \\ & + F_{x\_21}\cos\delta_{21} + F_{y\_21}\sin\delta_{21} + F_{x\_22}\cos\delta_{22} + F_{x\_22}\sin\delta_{22} \end{aligned} \tag{4}$$

$$\begin{aligned} ma_y = {} & F_{x\_11}\cos\delta_{11} + F_{y\_11}\sin\delta_{11} + F_{x\_12}\cos\delta_{12} + F_{y\_12}\sin\delta_{12} \\ & + F_{x\_21}\cos\delta_{21} - F_{y\_21}\sin\delta_{21} + F_{x\_22}\cos\delta_{22} - F_{x\_22}\sin\delta_{22} \end{aligned} \tag{5}$$

$$\begin{aligned} \Gamma = {} & a(F_{x\_11}\cos\delta_{11} + F_{y\_11}\sin\delta_{11}, -\tfrac{t_f}{2}(F_{x\_11}\cos\delta_{11} - F_{y\_11}\sin\delta_{11}) \\ & + a(F_{x\_12}\cos\delta_{12} + F_{y\_12}\sin\delta_{12}) + \tfrac{t_f}{2}(F_{x\_12}\cos\delta_{12} - F_{x\_12}\sin\delta_{x\_12}) \\ & + b(F_{x\_21}\cos\delta_{21} - F_{y\_21}\sin\delta_{21}) - \tfrac{t_r}{2}(F_{x\_21}\cos\delta_{21} + F_{x\_21}\sin\delta_{21}) \\ & + b(F_{x\_22}\cos\delta_{22} - F_{y\_22}\sin\delta_{22}) + \tfrac{t_r}{2}(F_{x\_22}\cos\delta_{22} + F_{x\_22}\sin\delta_{22}) \end{aligned} \tag{6}$$

where F_{x_ij} is the four-wheel longitudinal force, F_{y_ij} is the four-wheel lateral force, δ_{ij} is the four-wheel angle, m is the total mass, a and b represent the distance between the center of mass and the front and rear axles, respectively, t_f and t_r represent the distance of front and rear wheel distance, respectively, $j = 1$ or 2 is the left wheel and right wheel, respectively.

The longitudinal force of the tire can be obtained directly by using the four-wheel drive torque and angular acceleration obtained from the vehicle model and calculated through the wheel's motion moment balance equation, as shown in Formula (7):

$$F_{x\_ij} = \frac{T_{ij} - J_{ij}\cdot\omega_{ij}}{R_e} \tag{7}$$

where T_{ij} is the driving torque of each wheel, ω_{ij} is the angular acceleration of the four-wheel, R_e is the wheel radius, J_{ij} is the moment of inertia of each wheel, $i = 1$ or 2 is the front wheel and rear wheel, respectively, $j = 1$ or 2 is the left wheel and right wheel, respectively.

2.2. Tire Model

At present, there are many different tire models, among which the magic tire formula and the Dugoff tire model are widely used by researchers. Magic tire is an empirical formula based on multiple fitting parameters. Adding too many fitting parameters makes it difficult

to establish a close mathematical relationship between vehicle condition parameters and the magic tire formula.

This paper chooses the Dugoff tire model with relatively few parameters. From Formula (8), we can see that the main reason for choosing the tire model is that the capability to decouple the road surface adhesion coefficient is highly advantageous for the subsequent development of an algorithm designed to estimate the road surface adhesion coefficient. The requisite tire lateral force can be derived from the correlation between the lateral force and the slip rate, as illustrated in the equations provided below [27]:

$$F_{y\_ij} = u_{ij} F_{z\_ij} C_y \frac{\tan(\alpha_{ij})}{1-\lambda_{ij}} f(L) \tag{8}$$

$$f(L) = \begin{cases} L\cdot(2-L), L < 1 \\ 1, L \geq 1 \end{cases} \tag{9}$$

$$L = \frac{1}{\sqrt[2]{C_x^2\lambda_{ij}^2 + C_y^2 \tan^2 \alpha_{ij}}} (1-\lambda_{ij}) \times (1 - \varepsilon \cdot u_{ij} \cdot \sqrt{C_x^2\lambda_{ij}^2 + C_y^2 \tan^2 \alpha_{ij}}) \tag{10}$$

The lateral deflection angle of the four wheels can be calculated using Formulas (11) and (12).

$$\alpha_{11,12} = \delta_{11,12} - \arctan(\frac{v + ar}{u \pm \frac{t_f}{2} r}) \tag{11}$$

$$\alpha_{21,22} = \delta_{21,22} - \arctan(\frac{-v + br}{u \pm \frac{t_r}{2} r}) \tag{12}$$

The formula for calculating the tire's normal force is presented as follows:

$$F_{z\_11,12} = (\frac{1}{2} mg \pm ma_y \frac{h}{t_f}) \frac{b}{l} - \frac{1}{2} ma_x \frac{h}{l} \tag{13}$$

$$F_{z\_21,22} = (\frac{1}{2} mg \pm ma_y \frac{h}{t_r}) \frac{b}{l} + \frac{1}{2} ma_x \frac{h}{l} \tag{14}$$

The respective values of the slip rate of braking and driving are:

$$\begin{cases} \lambda_{ij} = \frac{R_e\omega_{ij} - v_{ij}}{v_{ij}} = \frac{R_e\omega_{ij}}{v_{ij}} - 1 (Brake) \\ \lambda_{ij} = \frac{v_{ij} - R_e\omega_{ij}}{v_{ij}} = 1 - \frac{R_e\omega_{ij}}{v_{ij}} (Drive) \end{cases} \tag{15}$$

$$\begin{cases} v_{11,12} = \sqrt{(u \pm \frac{t_f}{2} r)^2 + (v + ar)^2} \\ v_{21,22} = \sqrt{(u \pm \frac{t_r}{2} r)^2 + (v - br)^2} \end{cases} \tag{16}$$

where μ_{ij} is the road surface adhesion coefficient of four-wheel, λ_{ij} is the slip rate of the four-wheel, C_x is the longitudinal stiffness of the tire, C_y is the lateral stiffness of the tire, α_{ij} is the lateral deflection angle of the four-wheel, v_{ij} is the linear speed of four-wheel, F_{z_ij} is the tire normal force of four-wheel, ε is the speed influence coefficient, l is wheelbase, h is centroid height.

In addition, Formula (8) reveals that, within the context of the tire model, the accuracy of tire stiffness also has a non-negligible impact. Although there are many factors that will affect the value of tire stiffness, this paper will ignore other factors and calculate the cornering stiffness only for the load, which is the most important factor. Referring to the method described in reference [28], the stiffness of the tire can be calculated by the following formulas, respectively:

$$\begin{cases} C_{xij}(F_z) = m_1 F_{z\_ij} - n_1 F_{z\_ij}^2 \\ C_{yij}(F_z) = m_2 F_{z\_ij} - n_2 F_{z\_ij}^2 \end{cases} \tag{17}$$

where m_1, m_2, n_1 and n_2 are expressed as coefficients of second-order polynomials, respectively.

By extracting the data from the tire model developed in the simulation software CarSim (CarSim2019.0) and fitting it, the tire stiffness can be obtained directly. Figure 2 illustrates the relationship between longitudinal force and slip rate under different vertical loads. Figure 3 illustrates the relationship between lateral force and lateral deflection angle under different vertical loads.

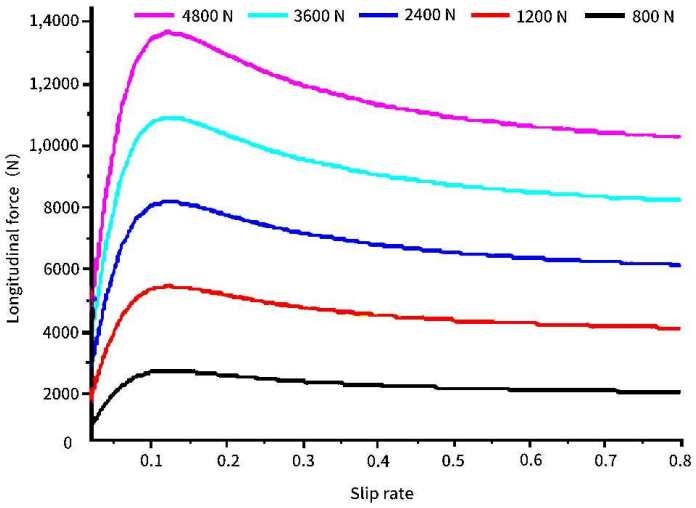

Figure 2. Longitudinal slip characteristic diagram.

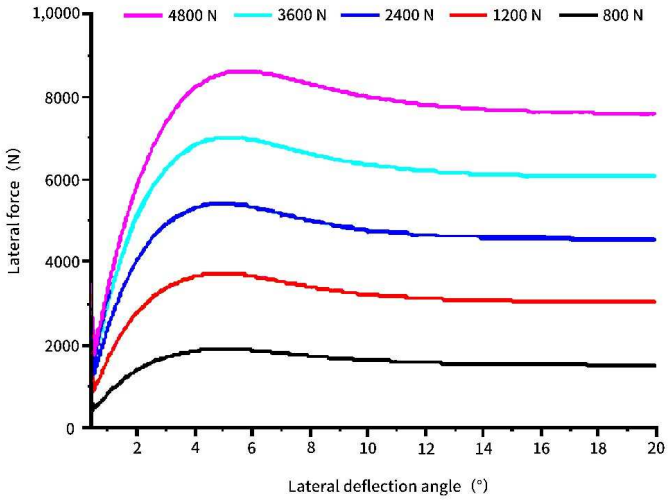

Figure 3. Lateral deflection characteristic diagram.

2.3. Vehicle Estimation Model

According to the established vehicle dynamics model, the following are selected:

State variables: $X_{si,k} = [u, v, a_x, a_y, \gamma, \Gamma]$.

Control input variables: $U_{s,k} = [\delta_{11}, \delta_{12}, \delta_{21}, \delta_{22}, \omega_{11}, \omega_{12}, \omega_{21}, \omega_{22}]$.

Combined with the tire model and the racing state estimation algorithm, the state equation and measurement equation of the estimation model are established and are shown below:

$$\begin{cases} X_{si,k} = f(X_{si,k-1}, U_{si,k-1}, W_{si,k-1}) \\ Z_{si,k} = h(X_{si,k}, v_{si,k}) \end{cases} \tag{18}$$

where W represents the process noise of the state equation and represents the measurement noise of the measurement equation, which is usually represented by the covariance matrices Q and R.

The relationship between the center of mass lateral deflection angle and the longitudinal acceleration and lateral speed of the vehicle is as follows:

$$\beta = \arctan\frac{v_y}{v_x} \tag{19}$$

2.4. CarSim Simulation Model

The accuracy of parameters is very important for vehicle simulation results to ensure that the parameters of the vehicle, such as tire radius, steering angle, speed, suspension stiffness, body quality, and so on, are accurate. The aforementioned parameters hold significant importance for the precision of the model and exert a direct influence on the accuracy of the simulation outcomes. The A-class model of the CarSim (CarSim2019.0) body model is selected in this paper, and the parameters at the simulation model interface are modified in accordance with the specifications of the actual vehicle. The settings for the simulation interface are depicted in Figure 4, and the real car parameters are shown in Table 1.

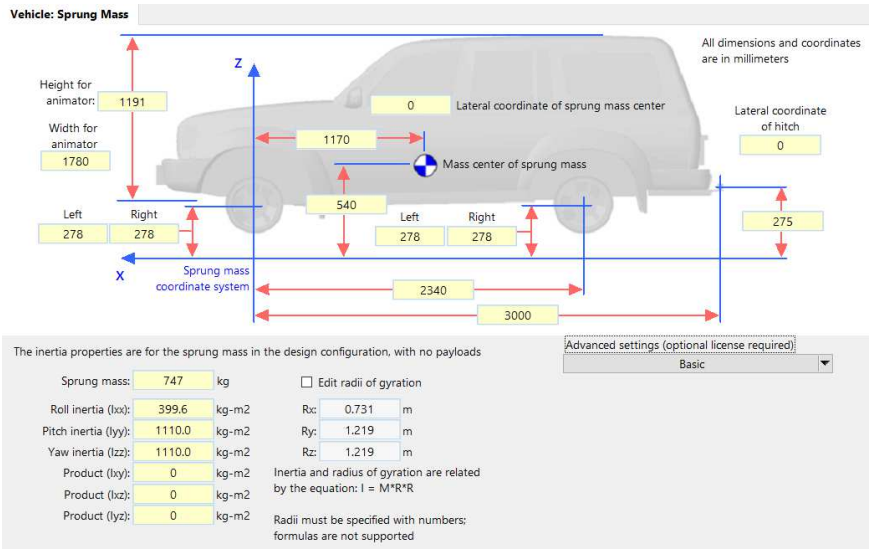

Figure 4. Body parameters in CarSim software (CarSim2019.0).

Table 1. Main parameters of the vehicle model.

Vehicle quality (kg)	m	830
Spring-loaded mass (kg)	m_s	747
Wheelbase (m)	L	2.34
Distance from the center of mass to the front axis (m)	A	1.17
Front-wheel distance (m)	d1	1.416
Rear wheel distance (m)	d2	1.416
Wheel radius (m)	r	0.278
Distance from centroid to ground (m)	h	0.54
Moment of inertia (kg·m^2)	Iz	1110
Tire longitudinal stiffness (n/m)	Cx	--
Tire lateral stiffness (n/m)	Cy	--

The vehicle model libraries of the CarSim software (CarSim2019.0) are full of conventional fuel vehicles, so the drive systems of the vehicles need to be remodeled. The drive system of a four-wheel independent drive and steering electric vehicle requires disengaging the original power transmission in CarSim (CarSim2019.0) and changing all modules to external input, as shown in Figure 5.

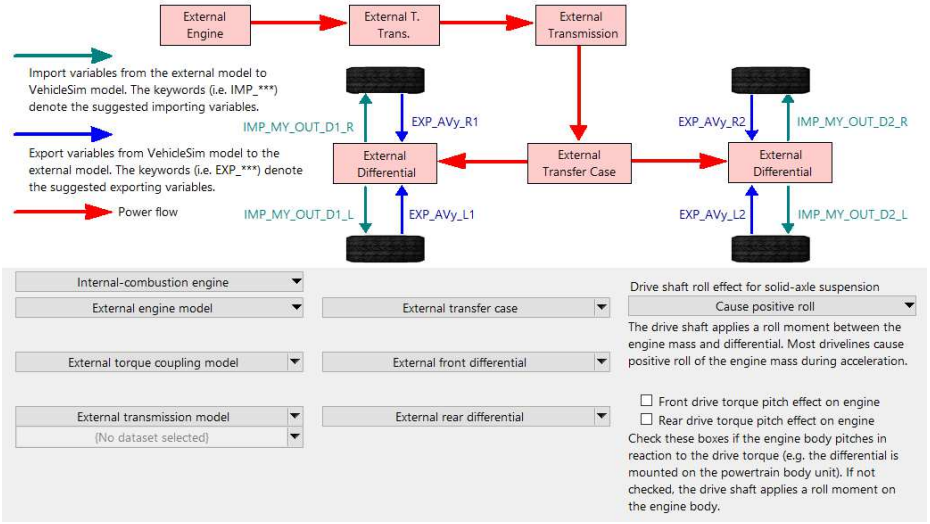

Figure 5. Settings of the drive system.

The torque of a four-wheel independent drive and steering electric vehicle can be distributed in two ways: equal drive torque and differential drive. The control program DYC reallocates the output torques of the four motors to achieve the required additional crossover torque. The output torque of its four motors can be adjusted individually to obtain different torque values. The drive motor model, employing PI control, outputs the actual four-wheel drive torque based on the torque commands from the drive control system, thus finalizing the control process. In this paper, the Simulink software (MATLAB2023a) is used to build the external motor and other models to establish the vehicle simulation model of the four-wheel independent drive electric vehicle.

In this paper, the four-wheel steering control strategy chooses the proportional four-wheel steering control strategy [29], in which the proportional coefficient is dependent on the vehicle speed and the function is expressed as Formula (20):

$$k = \frac{\delta_r}{\delta_f} = \frac{-b + [\frac{ma}{k_2(a+b)}]u^2}{a + [\frac{mb}{k_1(a+b)}]u^2} \tag{20}$$

3. Driving State Estimation

Vehicle driving state parameters, including longitudinal and lateral speed and the center of mass deflection angle, are crucial input parameters of the active control system. Because of measurement accuracy and cost, it is not easy to obtain their parameters. As a result, many advanced vehicle control algorithms cannot be realized in practice, so it is essential to develop an estimation algorithm corresponding to vehicle sensor configuration to obtain state parameters. In response to this problem, the paper makes full use of the structural advantages of electric vehicles with four-wheel independent drive and steering, incorporating the idea of federal filtering and the volume Kalman filter estimation algorithm. Real-time and accuracy problems are considered in many aspects when designing the vehicle driving state parameter estimation algorithm. In order to further optimize the structure of the estimator, targeted improvements are made on the basis of it. At the same time, using CarSim (CarSim2019.0) and MATLAB/Simulink software (MATLAB2023a), three typical representative working conditions are selected to verify the different performances.

3.1. Federal Filter Design Based on Distributed Fusion

Compared with the centralized fusion architecture, the distributed architecture system has the advantages of high feasibility, fast computing, excellent reliability, and sustainability. The volume Kalman filter has superiority for state estimation of high-dimensional nonlinear

dynamic systems and can provide higher estimation accuracy. Therefore, based on the distributed information fusion architecture, the internal sub-method uses volume Kalman filter theory to design a vehicle driving state estimation algorithm.

3.1.1. Federal Kalman Filter Principle

Federal Kalman filter (FKF) is a multi-sensor fusion technology. Its basic idea is to maintain the Kalman filter of each sensor and update the estimated state information regularly. In each update step, the state estimates of different sensors are fused according to the confidence of each sensor. FKF is a two-stage decentralized filter [30], which includes several sub-filters and main filters. The core principle is the idea of "information distribution". Because of its high accuracy and robustness, it is mostly used in military, positioning, integrated navigation, and other fields.

The workflow of federated filter: first, according to a certain allocation principle, the information of the system is distributed between the sub-filter and the main filter; that is, the process information of the system, the system noise matrix, and the state information of the fusion center are used to reset the state estimation of each filter; secondly, the time update process is carried out independently between each sub-filter and the main filter. Finally, when the sub-filter completes the measurement update, the respective system information is transmitted to the main filter for information integration.

3.1.2. Volume Kalman Filter Theory

In order to overcome the problem of low filtering accuracy in high-dimensional cases, Canadian scholars Arasaratnam and Haykin proposed a volume Kalman filter (CKF) for the first time in 2009. For the nonlinear filtering problem under a Gaussian distribution, the integral of a posteriori expectation is actually obtained. CKF approximates the posterior mean and covariance with additional Gaussian noise based on the integral transformation of third-order spherical radial rules. It is the closest algorithm to Bayesian probability distribution at present. Its essence is to solve the problem of nonlinear system filtering and the integral calculation of the Gaussian distribution [31].

The CKF algorithm is a suboptimal filter based on the Bayesian filtering theory framework. According to the prior mean and covariance, the volume point is selected by the volume rule, and the state posterior mean and covariance are obtained through the weighted processing of the volume point after the transfer of the nonlinear function. The analysis has the following characteristics:

(1) CKF is highly scalable, can be applied to a variety of three-dimensional space or volume estimation problems, and can be adapted by adjusting the parameters of the system model.
(2) There is no need to approximate the nonlinear system, so it is not limited by the specific form of the nonlinear system, and it is suitable for almost any form of nonlinear system within the allowable range of error. CKF has a greater advantage in nonlinear filtering because of its high efficiency in calculating multidimensional function integrals.
(3) The performance of CKF depends largely on the parameters of the filter, including the variance of process noise, the variance of measurement noise, and the initial state error. It is usually assumed that the correlation between the measurement and the system state is known and that the noise is Gaussian-independent and identically distributed. For non-Gaussian noise, other algorithms may be needed. Therefore, it is necessary to optimize the combination according to the characteristics of the actual problem.

3.2. Improved Design of Sub-Filters Based on Robust Estimation

Volume Kalman filtering is a nonlinear filtering method based on Bayesian estimation as the logical framework. Even in the filtering calculation of nonlinear systems in high-dimensional state space, the filtering weight is always positive and has higher filtering accuracy. However, the algorithm usually assumes that the input data were accurate and

obeys a Gaussian distribution. In practical applications, due to the influence of sensor failure, environmental noise, or other non-ideal conditions, the traditional filter is often vulnerable to abnormal data, which may cause the estimated results to deviate from the real value, and then it has an impact on the vehicle's control accuracy and the performance of the decision-making system. The robust estimation theory is introduced into the sub-filter to enhance the robustness of state estimation.

Robust estimation is usually based on the variance inflation model, which assumes that outliers are caused by an increase in variance. The core idea of robust estimation is to minimize the impact of abnormal values on the overall estimation by giving different weights to different observations in the estimation process. Applying this idea to vehicle driving state estimation, in the improved robust volume Kalman filter, the modified matrix of noise measurement variance is defined as $\overline{R}_{k+1} = \overline{P}^{-1}$. The equivalent weight matrix is P. The minimization function for calculating the equivalent weight matrix is as follows:

$$\overline{R}_{k+1} = \overline{P}^{-1} \tag{21}$$

$$J(x_k) = \sum_{i=1}^{2n} \rho(r_i) \tag{22}$$

where r_i is expressed as the component of the ith residual vector, its standard deviation is calculated, and the core function $\rho(r_i)$ is defined as follows:

$$r_i = (z_{k+1} - z_{k+1|k})_i \tag{23}$$

$$\sigma_{ri} = (P_{zz,k+1|k})_{i,i} \tag{24}$$

$$\rho(r_i) = \begin{cases} \frac{1}{2} r_i^2 & |r_i| \leq c \\ c\left|r_i\right| - \frac{1}{2}c^2 & |r_i| > c \end{cases} \tag{25}$$

Set the local deviation to zero.

$$\sum_{i=1}^{2n} \frac{\partial \rho(r_i)}{\partial (r_i)} \cdot \frac{\partial (r_i)}{x_{k,j}} \quad i = 1, 2, \cdots n \tag{26}$$

where $X_{k,i}$ is the component of the ith state vector, and the calculation equation can be obtained from the following equation:

$$w_i = \begin{cases} 1 & |r_i| \leq c \\ \frac{c}{|r_i|} & |r_i| > c \end{cases} \tag{27}$$

In summary, the formulas for calculating the equivalent weight matrix P, namely Formulas (28) and (29), can be obtained.

$$\overline{P}_{i,i} = \begin{cases} \frac{1}{\sigma_{i,i}} & \left(\left|\frac{r_i}{\sigma_{ri}}\right| = |r_i| \leq c\right) \\ \frac{c}{\sigma_{i,i}\left|r_{i,i}\right|} & (|r_i| > c) \end{cases} \tag{28}$$

$$\overline{P}_{i,j} = \begin{cases} \frac{1}{\sigma_{i,j}} & (|r_i| \leq c, \left|r_j\right| \leq c) \\ \frac{c}{\sigma_{i,j}\max(\left|r_i\right|, \left|r_j\right|)} & (|r_i| > c, (\left|r_j\right| > c) \end{cases} \tag{29}$$

Because the measurement noise variance matrix in vehicle driving state estimation is a diagonal matrix, the non-diagonal element in the matrix is zero, then σ_{ij} is zero, r_i is the corresponding residual component of the measured z_i, σ_i is the mean square error of r_i and c is an undetermined constant.

3.3. Research on Driving State Estimation Based on Intelligent Antlion Optimization

In the estimation of driving states, the impacts exerted by measurement noise and process noise on the estimation algorithm cannot be ignored, and the existence of these two kinds of noise may introduce errors, thus reducing the accuracy and reliability of the estimation. Measurement noise mainly comes from the collection and processing of sensor data. Process noise mainly originates from the uncertainty and nonlinear characteristics of the vehicle dynamics model. Therefore, there is a certain difference between the model and the actual situation, and this difference will introduce a certain amount of noise in the estimation process. The greater the noise in the system process, the more the performance of the designed estimation algorithm depends on the feedback correction of the measurement update process.

It is assumed that the non-Gaussian noise and bad data after robust estimation are completely filtered out. So as to improve the accuracy of the federal filter driving state estimator, when discussing the noise processing results of a vehicle nonlinear system, both the process and measurement noises conform to a Gaussian distribution, the antlion optimization algorithm is introduced to identify the statistical characteristics of process and measurement noise, presuming a Gaussian hypothesis.

3.3.1. Antlion Optimization Algorithm

The Antlion optimization algorithm is a naturally inspired intelligent optimization algorithm to solve optimization problems. As the designation suggests, the antlion optimization algorithm replicates the predatory tactics of antlions in their natural pursuit of ants. Because its algorithm integrates random walks, roulette strategies, elite strategies, and other thinking strategies, the ALO algorithm becomes a search technology with strong optimization performance and is easy to implement. Compared with other popular intelligent algorithms, such as the Beetle Antennae Search Algorithm (BAS), Grey Wolf Optimizer (GWO), and Sparrow Search Algorithm (SSA), the AntLion optimization algorithm shows better convergence, accuracy, and robustness.

In the antlion optimization algorithm, the antlion is equivalent to the solution of the optimization problem, while the ant represents the candidate solution in the search space. In the antlion optimization algorithm, the random walk of ants can ensure the global search, while the roulette strategy and elite strategy ensure the optimization performance of the algorithm. A roulette strategy is a probability selection strategy based on fitness value, which makes ants with high fitness have more chances to be selected as the next generation of ants so as to achieve the preservation of excellent genes. The elite strategy is to retain a certain number of ants with the highest fitness in each iteration to prevent the algorithm from falling into the local optimal solution.

The implementation of the ALO algorithm is based on selecting a random walk to simulate the movement of ants, setting a fitness function during the optimization process, and storing the fitness value of the ants. The algorithm continuously learns from elite ant lions, and the ants constantly update the step size and direction of their random walks to make sure the algorithm is always looking for the best solution. Figure 6 illustrates the operational sequence of the ALO algorithm.

The specific steps mainly include the following:

(1) Initialization: set algorithm parameters, such as population size, number of iterations, search space, etc., and randomly generate an initial population.
(2) Foraging ant random walk: simulate the random walk behavior of ants in the foraging process. According to the random walk formula, calculate the position of each ant in the search space and normalize it.
(3) Setting traps: antlions dig funnel-shaped traps in sandy soil and hide at the bottom of the trap to wait for prey. In the ALO algorithm, the position and shape of the trap can be set through certain strategies, such as adjusting based on historical search information or the current optimal solution.

(4) Trapping ants with traps: when ants randomly walk into a trap, ant lions quickly prey on them. In the algorithm, when the position of an ant meets the conditions of the trap, the ant is considered to be captured, and it is processed, such as updating its position or adding it to the elite population.

(5) Catching prey and rebuilding traps: after antlions prey on ants, they will repair the traps and wait for the next hunt. In the algorithm, when a certain number of ants are captured, the trap can be reconstructed to update the search space and population distribution.

(6) Iterative updates: repeat steps 2–5 until the preset number of iterations or other termination conditions are met. In each iteration, the location and distribution of the population are updated according to the interaction between ants and ant lions, so as to achieve global optimization.

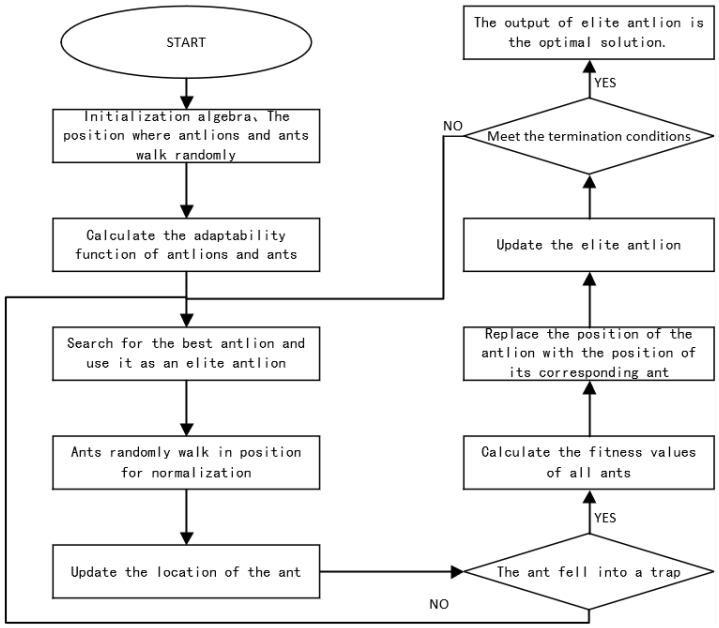

Figure 6. Flow chart of the ALO algorithm.

3.3.2. Design of an Antlion-Federal Kalman Filter Estimator

The noise statistical characteristics of the FKF algorithm are identified by the ALO algorithm. With the design of the antlion-volume Kalman filter (ALO-FKF) state parameter estimation algorithm, it is presumed that non-Gaussian noise and bad data after the tolerance estimate have been completely removed. In other words, it is assumed that the measurement noise and process noise of the vehicle nonlinear system are Gaussian noise with a zero mean. Within the FKF driving state parameter estimation framework, the covariance matrices Q and R are diagonally positive definite matrices.

State variables: $X_{si,k} = [u, v, a_x, a_y, \gamma, \Gamma]$.

Measurement variables of the sub-filter: $Z_{s1,k} = [a_x, a_y, \gamma]$.

Control input variables: $U_{s,k} = [\delta_{11}, \delta_{12}, \delta_{21}, \delta_{22}, \omega_{11}, \omega_{12}, \omega_{21}, \omega_{22}]$.

According to the established vehicle estimation model, the state space equation includes six state variables and three measurement variables, and the covariance matrices can be defined as follows:

$$\begin{cases} Q = diag(q_1, q_2, q_3, q_4, q_5, q_6) \\ R = diag(r_1, r_2, r_3) \end{cases} \tag{30}$$

Merge the covariance matrices Q and R into a vector to be optimized, as follows:

$$F_t(y_j^t) = \sum_{k=1}^{M} \sum_{i=1}^{3} W_i (z_{i,k} - \hat{z}_{i,k}(\hat{y}_j^t))^2 \tag{31}$$

where $Z_{i,k}$ is the true value of the i measurement variable at the k time, and $\hat{Z}_{i,k}(\hat{y}_j^t)$ is the estimated value of the j antlion at the k time at the t iteration.

The schematic diagram of the vehicle driving state parameter estimator is shown in Figure 7.

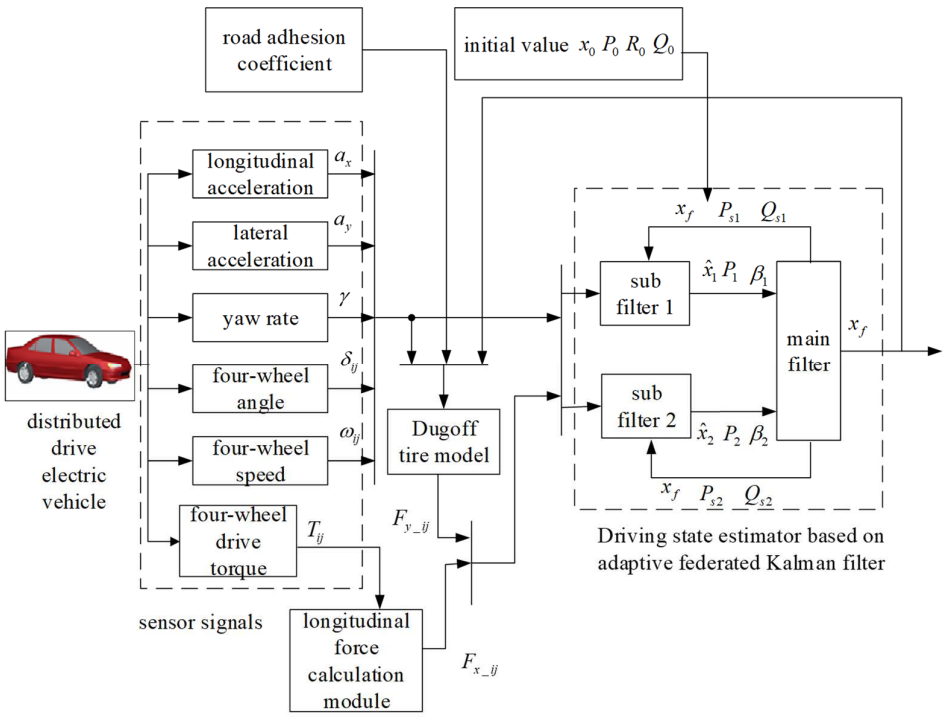

Figure 7. Schematic diagram of driving state estimation.

The procedure for estimating the driving state is as follows: The principal input consists of the sensor output data from the vehicle simulation model. The road surface adhesion coefficient is set to a fixed value and input into the tire model. The lateral force of a tire is determined by the relationship between the adhesion coefficient and the lateral force. At the same time, according to the formula of four-wheel drive torque and longitudinal force, the tire's longitudinal force can be directly calculated and subsequently employed as another input for the vehicle's driving state estimator.

After receiving each signal input, first initialize the main filter, complete the distribution of the input information, and input the variable parameters, error covariance matrix, and process noise covariance matrix into each sub-filter. Every sub-filter integrates all the assigned parameter signals and sensor signals and completes the time update and measurement update, respectively, by utilizing the volume Kalman filter principle, thereby obtaining posterior local estimation values, which are then relayed back to the main filter. The main filter fuses the signals fed back by the respective local filters. The information distribution coefficient is recalibrated based on the confidence level of the data transmitted by each sub-filter and subsequently redistributed to every local filter within the main filter. At the same time, the error covariance matrix and process noise covariance matrix are transmitted to the antlion optimization module, and then they are optimized and returned to each local filter. To maintain real-time performance, the feedback before the end of optimization still uses the allocation signal of the main filter. So far, an iterative process has been completed. Finally, the main filter fuses the information of each feedback signal and

outputs the estimated value, which is constantly fed back to the input module as the output, and the model parameters are then adjusted to establish a comprehensive closed-loop feedback system. The precise estimation of longitudinal and lateral speed, as well as the lateral deflection angle of the center of mass, is achieved.

3.3.3. Verification by Simulation Experiment

First of all, the typical working conditions of a double shift line that reflect the evaluation of vehicle stability are selected to verify, and then the angle step condition and sinusoidal condition are selected, respectively. In the angle step condition, the vehicle enters the non-zero steady state after the transient response to verify the steady-state estimation effect of the estimator. The sinusoidal condition can mirror the vehicle's driving performance under conditions of sustained emergency steering and stimulate the dynamic performance of the vehicle to verify the dynamic estimation effect of the estimator [32].

(1) Double shift line condition.

The test scenario involves a double-lane change on a surface with an adhesion coefficient of 0.5, where the vehicle's speed is set at 35 km/h and data were sampled at a constant rate of 0.002 s.

Figure 8 presents a comparative analysis of the estimated driving state parameter values and the actual values obtained based on the two estimation algorithms of federal Kalman filtering and improved antlion federal Kalman filtering.

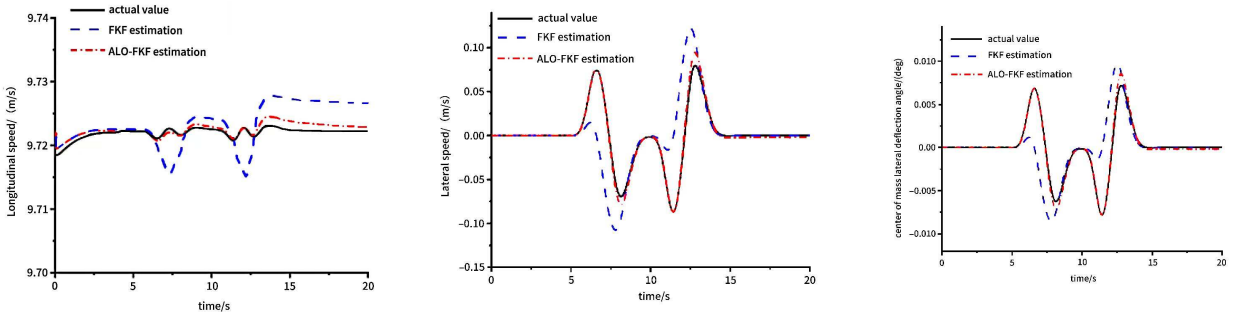

(**a**) (**b**) (**c**)

Figure 8. Algorithm comparison: (**a**) Longitudinal speed; (**b**) Lateral speed; (**c**) Center of mass lateral deflection angle.

Figure 8a illustrates the comparison of the estimation results of the longitudinal speed, and it can be seen that the results of the improved antlion Federal Kalman Filter estimator are significantly optimized over the pre-improved one, with better tracking capability and accuracy. By comparing the estimation results of lateral vehicle speeds in Figure 8b, it is obvious that except for a small deviation at the peak value of about 13 s, the other curves of the improved algorithm are basically consistent. Figure 8c shows the estimated value of the lateral deflection angle of the center of mass, and the result is a top priority of the estimation algorithm. It is clear from the curves that the estimates obtained using the improved Antlion Federal Kalman Filter algorithm hold up well in overall estimation, except for smaller errors at the peaks and valleys that are within the range of practical engineering applications.

This paper quantitatively compares the estimation error of the center of mass lateral deflection angle between the two algorithms. The calculation method of reference [33], that is, the mean absolute error (MAE) and root mean square error (RMSE), are computed for the estimates in relation to the actual values, with the findings presented in Table 2.

From the data in Table 2, it is more evident that the estimation error for the vehicle driving state achieved through the use of the enhanced Antlion federal Kalman filter algorithm is smaller. In comparison to the estimation algorithm founded on the federal

Kalman filter theory, it has higher accuracy. The feasibility of the Antlion Federal Kalman Filter estimation algorithm is substantiated through verification.

Table 2. MAE and RMSE indexes of simulation results of two algorithms.

		Longitudinal Speed	Lateral Speed	Center of Mass Lateral Deflection Angle
MAE	FKF	0.0050	0.0274	0.0025
	ALO-FKF	0.0008	0.0024	0.0002
RMSE	FKF	0.0063	0.0572	0.0052
	ALO-FKF	0.0010	0.0040	0.0003

(2) Low attachment steering wheel angle step input.

Under this working condition, the vehicle's driving speed is adjusted to 40 km/h, and the road surface adhesion coefficient is set at 0.3. Throughout the process, a turning angle with an amplitude is introduced to the steering a turning angle with an amplitude of 1 radian is introduced to the steering wheel at the 5-s interval, and the vehicle enters a non-zero steady state after the transient response, which can be better used to verify the steady-state estimation effect of the estimator.

Analyzing the simulation results, overall it can be found that the steady-state estimation effect of the estimator is good when the vehicle enters the non-zero steady state after the transient response under the angle step condition. Among them, Figure 9a illustrates a comparative analysis of the longitudinal speed estimation outcomes derived from the two distinct estimation algorithms. Visual inspection reveals that the estimation effect of the improved antlion federal Kalman filter estimator after 8 s is significantly optimized compared to that before improvement and has better accuracy. Figure 9b presents a comparative view of the lateral speed estimation results. It is obvious that the results of the two algorithms are basically the same in about 10 s and then influenced by the augmented steering wheel angle. The improved algorithm makes up for the error of the FKF algorithm. The estimation of the center of mass lateral deflection angle is shown in Figure 9c, which is a paramount aspect of the algorithm's output. After about 8 s, the output of the improved antlion federal Kalman filter algorithm begins to converge to the actual value, the real value after about 4 s, and gradually maintains stability. The discrepancy between the estimated and actual value is very minimal; thus, this suggests that the estimation algorithm performs effectively. And the steady-state estimation effect of the estimator is good when it enters the non-zero steady state.

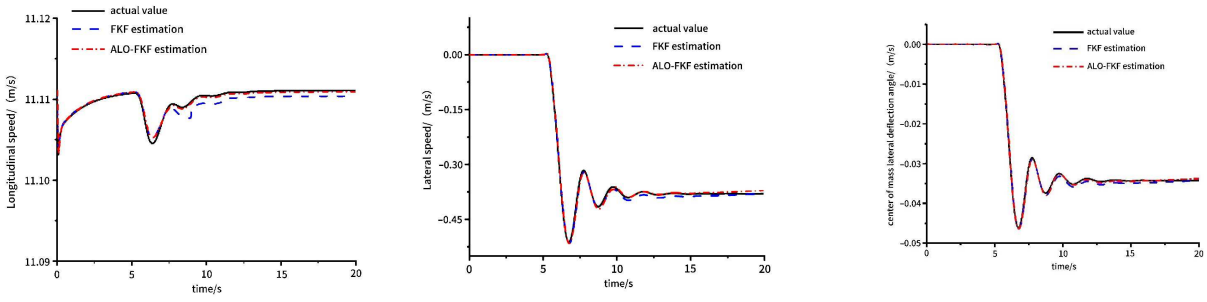

(**a**) (**b**) (**c**)

Figure 9. Algorithm comparison: (**a**) Longitudinal speed; (**b**) Lateral speed; (**c**) Center of mass lateral deflection angle.

(3) Sinusoidal input of a highly attached steering wheel.

This condition requires the road surface to have high adhesion performance; the road surface adhesion coefficient is adjusted to 0.8; the vehicle's traveling speed is set at

40 km; and a sinusoidal steering input is applied. The sinusoidal conditions can reflect the assessment of the vehicle's driving performance under sustained emergency steering scenarios, which can stimulate the dynamic performance of the vehicle and thus verify the dynamic estimation effect of the estimator as well as the accuracy and adaptability of the designed algorithms under the scenario of continuous turning.

Figure 10 shows a plot of the comparison between the estimated and actual driving state parameters obtained from two estimation algorithms grounded in the federal Kalman filter and the improved Antlion federal Kalman filter. Figure 10a depicts the comparative curve of longitudinal speed, and the graph indicates that it is easy to see that the estimation results obtained based on both algorithms produce more obvious errors whenever the steering wheel turning angle peaks, but the estimation value of the algorithm designed based on the improved Antlion federal Kalman filter theory has relatively better estimation accuracy and tracking capability. The graph illustrated in Figure 10b reveals that the estimated curve of lateral speed almost overlaps with the true value, and its tracking effect is better than that of the pre-improvement algorithm. The curve in Figure 10c shows that the lateral deflection angle of the center of mass, as estimated utilizing the improved federal Kalman filter algorithm, almost coincides with the true value curve, which maintains efficient tracking performance even in the case of continuous turning. The improved algorithm is superior not only in estimation accuracy but also in real-time tracking performance and stability.

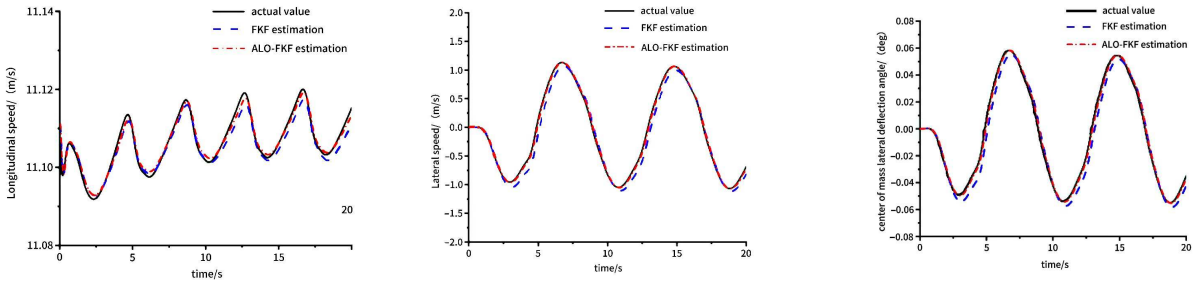

(**a**) (**b**) (**c**)

Figure 10. Algorithm comparison: (**a**) Longitudinal speed; (**b**) Lateral speed; (**c**) Center of mass lateral deflection angle.

4. Joint Estimation of Driving State and Road Surface Adhesion Coefficient

The road surface adhesion coefficient is an important parameter to measure the road surface resistance and vehicle traction capacity, which are closely bound up to the formulation of the vehicle braking control strategy, and the accurate identification of the road surface adhesion coefficient is an essential condition for the vehicle active control system, as it directly influences the effectiveness of the system in maintaining vehicle stability and preventing accidents. In the above estimation study, the road surface adhesion coefficient is set as a fixed value, while the real road condition in the driving process is complex and variable. Therefore, predicated on the functional interplay between the driving state parameters and the road surface adhesion coefficient, this chapter designs the road surface attachment coefficient estimator to form a double joint estimator, which facilitates the accurate estimation of the road surface adhesion coefficient and at the same time feeds back the information to the driving state estimator for continuous correction, so as to consider the dynamic characteristics of the road surface, thus enhancing adaptability and stability and enabling it to accommodate varying road conditions with heightened precision.

4.1. Joint Estimation Principle

First of all, in conjunction with the three degrees of freedom vehicle model, the relationship between the state parameters and the road surface adhesion coefficients is

determined, the parameter variables of the two estimators are determined, and the system's state and measurement equations are formulated as follows:

$$\begin{cases} X_{s/pi,k} = f(X_{s/pi,k-1}, U_{s/pi,k-1}, W_{s/pi,k-1}) \\ Z_{s/pi,k} = h(X_{s/pi,k}, v_{s/pi,k}) \end{cases} \tag{32}$$

Selection of variables in the driving state estimator:
State variables: $X_{si,k} = [u, v, a_x, a_y, \gamma, \Gamma]$.
Measurement variables: $Z_{s1,k} = [a_x, a_y, \gamma]$, $Z_{s2,k} = [a_y, \gamma]$.
Selection of variables in the road surface adhesion coefficient estimator:
Parameter variables: $X_{p,k} = [\mu_{11}, \mu_{12}, \mu_{21}, \mu_{22}]$.
Measurement variables: $Z_{p1,k} = [a_x, a_y, \gamma]$, $Z_{p2,k} = [a_y, \gamma]$.
Control input variables: $U_{s,k} = [\delta_{11}, \delta_{12}, \delta_{21}, \delta_{22}, \omega_{11}, \omega_{12}, \omega_{21}, \omega_{22}]$.

Secondly, the closed-loop design of each parameter feedback signal and joint estimation between the two estimators is determined; the schematic diagram of the principle is shown in Figure 11.

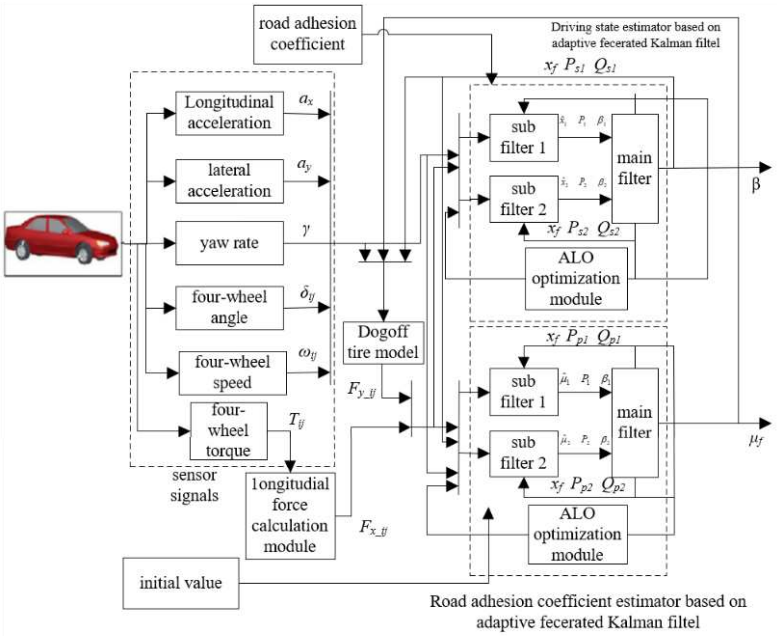

Figure 11. Joint estimation principle.

The joint estimation works as follows: the sensor data solved by the vehicle simulation model is used as an input signal and passed to the joint estimation model. Among them, signals such as longitudinal and lateral acceleration, yaw angular velocity, four-wheel speed, and driving torque are input to each filter and tire model. Signals such as four-wheel speed and driving torque are computed to determine the longitudinal force exerted on the four wheels within the tire longitudinal force calculation module, and the lateral force is calculated in the tire model. At the same time, the longitudinal or lateral force of the tire is used as another input for each filter. In the main filter, after receiving all kinds of initial signals, initialization and allocation are completed, and the variable parameters are input into each sub-filter. The initial value parameters are given in the following simulation conditions: Following the integration of all designated parameter signals by each sub-filter, the local estimated value is derived through a time update and measurement update based on the designed robust volume Kalman filter, which is output to the main filter. The main filter fuses information on the parameter variables, error covariance fed back by the respective local filters, and finally outputs the estimates. Within the main filter, according to the confidence level of the data transmitted by the sub-filters, the information allocation coefficients are readjusted, and the parameters of the variables, as well as the

error covariance and the process noise covariance matrix, are again returned to be allocated to the individual local filters in terms of the information allocation principle. At the same time, the error covariance matrix and the process noise covariance matrix are passed to the ALO optimization module, and then they are optimized and returned to each local filter. To guarantee real-time performance, the feedback before the optimization is still assigned by the main filter, and an iterative process is completed.

Different from a separate driving state estimator, the parameter estimates derived from the joint estimation algorithm facilitate real-time information exchange and feedback updating during continuous iteration. As a result, the road surface adhesion coefficient is dynamically adjusted rather than fixed, enabling it to align with the actual road conditions as required. Thus, the precision of the algorithm's estimation is significantly enhanced, and it finally obtains more accurate estimates of vehicle longitudinal speed, lateral speed, center of mass lateral deflection angle, and road surface adhesion coefficient.

4.2. Design of a Joint Estimation Algorithm

The explicit procedural steps of the estimation algorithm are delineated in the subsequent formula:

(1) Information distribution of the main filter

$$X_{si,k-1}^{\wedge} = X_{sf,k-1}, X_{pi,k-1}^{\wedge} = X_{pf,k-1} \tag{33}$$

$$P_{si,k-1}^{-1} = \beta_{si} P_{sf,k-1}^{-1}, P_{pi,k-1}^{-1} = \beta_{pi} P_{pf,k-1}^{-1} \tag{34}$$

$$Q_{si,k-1}^{-1} = \beta_{si} Q_{sf,k-1}^{-1}, Q_{pi,k-1}^{-1} = \beta_{pi} Q_{pf,k-1}^{-1} \tag{35}$$

(2) Time update of each sub-filter

① The error covariance matrix undergoes decomposition via singular value decomposition (SVD), and the volume points are calculated as follows:

$$P_{s,k-1} = A_{s,k-1} \Lambda_{s,k-1} A_{s,k-1}^{T}, \;\; P_{p,k-1} = A_{p,k/k-1} \Lambda_{p,k/k-1} A_{p,k/k-1}^{T} \tag{36}$$

$$X_{sj,k-1} = A_{si,k-1} S_{s,k-1} \xi_j + X_{s,k-1}^{\wedge}, \;\; X_{pj,k-1} = A_{pi,k-1} S_{pi,k-1} \xi_j + X_{p,k-1}^{\wedge} \tag{37}$$

② The new volume point is obtained by iterating the state transition equation:

$$X_{sj,k/k-1}^{*} = f(X_{sj,k,k-1}, U_k), X_{pj,k/k-1}^{*} = f(X_{pj,k,k-1}, U_k) \tag{38}$$

③ Predicted values of prior state parameters and error covariance matrix:

$$X_{s,k/k-1}^{\wedge} = \sum_{j=1}^{m} \frac{1}{m} X_{sj,k/k-1}^{*}, X_{p,k/k-1}^{\wedge} = \sum_{j=1}^{m} \frac{1}{m} X_{pj,k/k-1}^{*} \tag{39}$$

$$P_{s,k/k-1} = \sum_{j=1}^{m} \frac{1}{m} X_{sj,k/k-1}^{*} X_{sj,k/k-1}^{*T} - \hat{X_{s,k/k-1}} \hat{X_{s,k/k-1}^{T}} + Q_s \tag{40}$$

$$P_{p,k/k-1} = \sum_{j=1}^{m} \frac{1}{m} X_{pj,k/k-1}^{*} X_{pj,k/k-1}^{*T} - \hat{X_{p,k/k-1}} \hat{X_{p,k/k-1}^{T}} + Q_p \tag{41}$$

where Q_s and Q_p are process noise covariance matrices.

(3) Measurement update for each sub-filter

① Decomposition of the covariance matrix and calculation of volume points:

$$P_{s,k/k-1} = A_{s,k/k-1} \Lambda_{s,k/k-1} A_{s,k/k-1}^{T} \tag{42}$$

$$P_{p,k/k-1} = A_{p,k/k-1} \Lambda_{p,k/k-1} A_{p,k/k-1}^{T} \tag{43}$$

$$X_{sj,k/k-1} = A_{si,k/k-1} S_{si,k/k-1} \xi_j + \hat{X_{s,k/k-1}} \tag{44}$$

$$X_{pj,k/k-1} = A_{pi,k/k-1} S_{pi,k/k-1} \xi_j + \hat{X_{p,k/k-1}} \tag{45}$$

② The new volume points are calculated according to the measured variables:

$$Z_{sj,k/k-1} = h(X_{sj,k/k-1}, \hat{X_{sj,k/k-1}}, U(k)) \tag{46}$$

$$Z_{pj,k/k-1} = h(X_{pj,k/k-1}, \hat{X_{pj,k/k-1}}, U(k)) \tag{47}$$

③ Find the average:

$$\hat{Z_{sj,k/k-1}} = \sum_{j=1}^{m} \frac{1}{m} Z_{sj,k/k-1}, \hat{Z_{pj,k/k-1}} = \sum_{j=1}^{m} \frac{1}{m} Z_{pj,k/k-1} \tag{48}$$

④ Innovation variance:

$$P_{szz,k/k-1} = \sum_{j=1}^{m} \frac{1}{m} Z_{sj,k/k-1} Z_{sj,k/k-1}^T - \hat{Z_{s,k/k-1}} Z_{s,k/k-1}^T + \varepsilon_s R_s \tag{49}$$

$$P_{\mathrm{pzz},k/k-1} = \sum_{j=1}^{m} \frac{1}{m} Z_{pj,k/k-1} Z_{pj,k/k-1}^T - \hat{Z_{p,k/k-1}} Z_{p,k/k-1}^T + \varepsilon_p R_p \tag{50}$$

In Formulas (49) and (50), ε_s and ε_p are adjustment factors, and R_s and R_p are measurement noise covariance matrix.

⑤ Mutual covariance:

$$P_{sxz,k/k-1} = \sum_{j=1}^{m} \frac{1}{m} X_{sj,k.k-1} Z_{sj,k.k-1}^T - \hat{X_{s,k/k-1}} Z_{sj,k.k-1}^T \tag{51}$$

$$P_{pxz,k/k-1} = \sum_{j=1}^{m} \frac{1}{m} X_{pj,k.k-1} Z_{pj,k.k-1}^T - \hat{X_{p,k/k-1}} Z_{pj,k.k-1}^T \tag{52}$$

⑥ Filter gain:

$$K_{s,k} = P_{sxz,k/k-1} P_{szz,k/k-1}^{-1}, K_{p,k} = P_{pxz,k/k-1} P_{pzz,k/k-1}^{-1} \tag{53}$$

⑦ Corrected and updated state estimates and error covariance matrix:

$$\hat{X_{s,k}} = \hat{X_{s,k/k-1}} + K_{s,k}(Z_{s,k} - \hat{Z_{s,k/k-1}}) \tag{54}$$

$$\hat{X_{p,k}} = \hat{X_{p,k/k-1}} + K_{p,k}(Z_{p,k} - \hat{Z_{p,k/k-1}}) \tag{55}$$

$$P_{s,k} = P_{s,k/k-1} - K_{s,k} P_{szz,k/k-1} K_{s,k}^T \tag{56}$$

$$P_{p,k} = P_{p,k/k-1} - K_{p,k} P_{pzz,k/k-1} K_{p,k}^T \tag{57}$$

⑧ Robust adaptive distribution coefficient:

$$\hat{P}_k = \frac{1}{a_k}(1 - \overline{K}_k A_k) P_k \tag{58}$$

(4) Information Fusion of main filter

$$P_{sf,k}^{-1} = P_{s1,k}^{-1} + P_{s2,k}^{-1}, P_{pf,k}^{-1} = P_{p1,k}^{-1} + P_{p2,k}^{-1} \tag{59}$$

$$\hat{X_{sf,k}} = P_{sf,k}^{-1}(P_{s1,k}^{-1} \hat{X_{s1,k}} + P_{s2,k}^{-1} \hat{X_{s2,k}}) \tag{60}$$

$$\hat{X_{pf,k}} = P_{pf,k}^{-1}(P_{p1,k}^{-1}\hat{X_{p1,k}} + P_{p2,k}^{-1}\hat{X_{p2,k}}) \tag{61}$$

(5) Optimal update of covariance matrix:

$$F_t(\hat{y}_j^t) = \sum_{k=1}^{M}\sum_{i=1}^{3} W_i(z_{i,k} - \hat{z}_{i,k} - \hat{z}_{i,k}(\hat{y}_j^t))^2 \tag{62}$$

4.3. Simulation Experiment Verification

To validate the feedback effect of the road surface adhesion coefficient within the devised joint estimation algorithm, experiments are conducted under varying road surface conditions, and the opposite double shift line condition and steering wheel angle step input are selected, respectively.

4.3.1. Working Condition of Double-Shift Road Surface Opposite Each Other

Under this condition, the road's adhesion coefficients are different, which are set to 0.5 and 0.3, respectively. The road surface exhibits a relatively low traction coefficient. In order to prevent the car from slipping and other dangerous phenomena when the adhesion is low, a lower speed value should be selected, and the vehicle speed should be adjusted to 25 km/h.

Figure 12 is a comparison curve between the estimated results using the Antlion federal Kalman filter estimator and its true value. Among them, Figure 12a shows that the estimated value of the initial time can well track the real value. As the speed trend became more complex, it began to produce a small error, but within a reasonable range. It can be observed from Figure 12b that the estimated lateral speed derived from the enhanced algorithm closely aligns with the true value curve, displaying only minor discrepancies at peak values. Figure 12c shows the graph of the true value of the center of mass lateral deflection angle and the estimated value produced by the improved algorithm. The two curves are almost consistent, with only a minor deviation at the peak value, which meets the actual engineering needs. Figure 12d presents the comparative curve of the estimated road surface adhesion coefficient obtained through the antlion-federated Kalman filter algorithm versus the actual value preset in the experiment. It is evident that the overall estimated value quickly converges to near the true value within a brief time frame. However, due to the drive system's theoretical system, a significant error arises in the estimation of the front left wheel's road surface adhesion coefficient; nonetheless, the error is controlled within an acceptable range and complies with practical engineering standards. The simulation results of the open double-shift condition effectively confirm the effectiveness of the joint estimator designed for electric vehicles with four-wheel independent drive and steering.

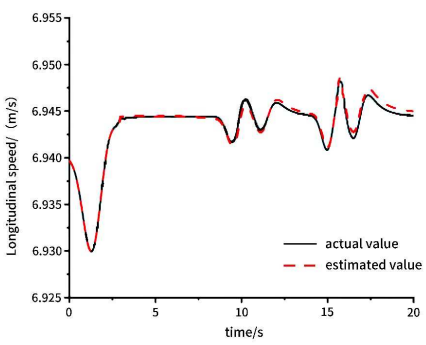

(**a**)

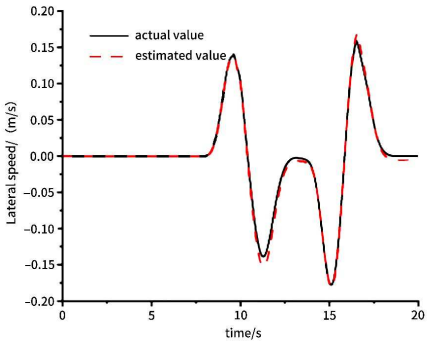

(**b**)

Figure 12. *Cont.*

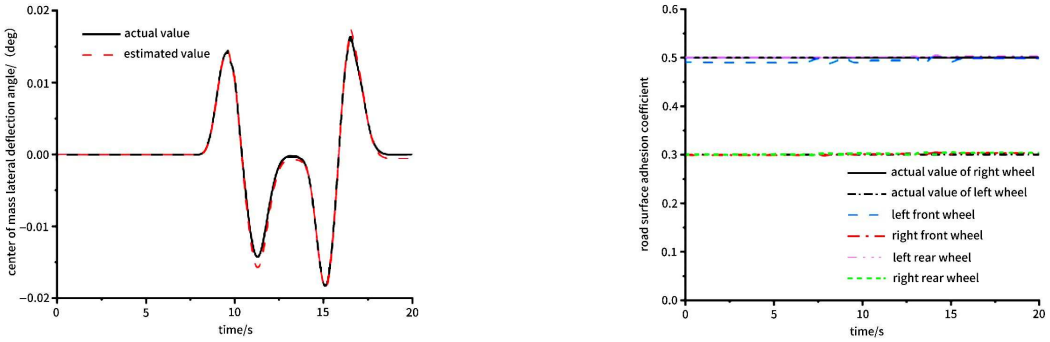

(**c**) (**d**)

Figure 12. Simulation results of the joint estimation algorithm: (**a**) Longitudinal speed; (**b**) Lateral speed; (**c**) Center of mass lateral deflection angle; (**d**) Road surface adhesion coefficient.

4.3.2. Serpentine Road Condition

This condition will stimulate the vehicle's dynamic performance, and the dynamic estimation effect of the estimator can be verified by choosing the road surface adhesion coefficient as 0.5 and the driving speed of the vehicle as 40 km.

Figure 13a shows the simulation estimation tracking results of the longitudinal speed. It can be seen that in the case of changing road conditions, using the improved Antlion federal Kalman filtering algorithm for estimating the actual value yields accurate tracking of the value. The estimation error exhibits a slight increase after 7 s but still remains within 0.3 percent, and the error is maintained within an acceptable range, meeting the practical requirements of the project. Figure 13b shows the graphs of the estimated lateral speeds versus the actual values; the trackability of the improved algorithm is consistent with the actual road conditions, and the estimation results are highly accurate. Figure 13c shows a plot of the estimated versus actual values of the center of mass lateral deflection angle, whose estimated values remain almost identical to the actual values. The resultant curve fits well in the first 7 s, after which a small error occurs with a gradual increase in time. Figure 13d shows the comparison results between the estimated road surface adhesion coefficient and the true value set by the simulation condition, and there is a small error between the estimated road surface adhesion coefficient and the actual value, which indicates that the estimation algorithm's effectiveness is superior and that it offers enhanced benefits in accuracy, stability, and real-time performance.

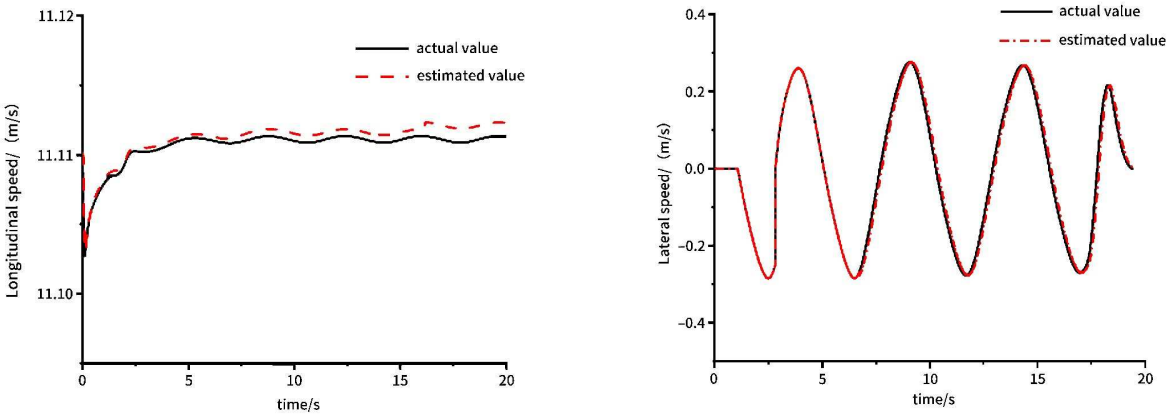

(**a**) (**b**)

Figure 13. *Cont.*

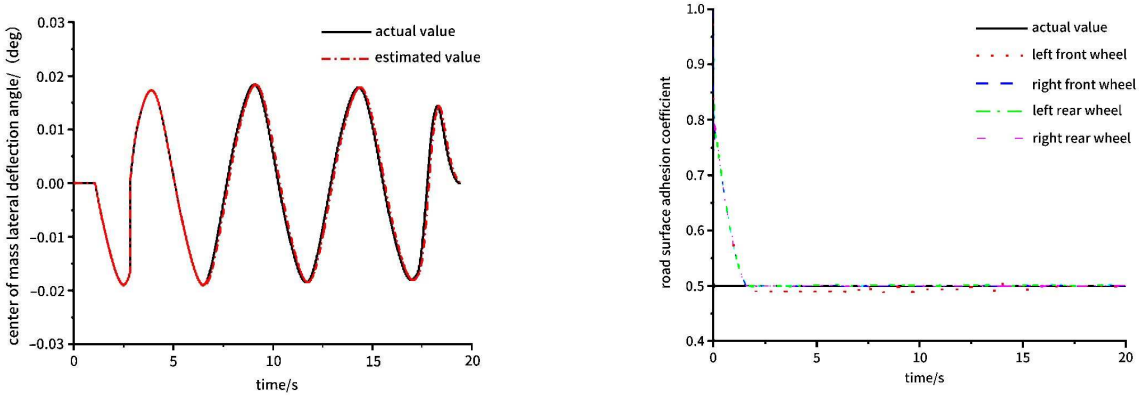

(**c**) (**d**)

Figure 13. Simulation results of the joint estimation algorithm: (**a**) Longitudinal speed; (**b**) Lateral speed; (**c**) Center of mass lateral deflection angle; (**d**) Road surface adhesion coefficient.

5. Discussion

The simulation results of the antlion federal Kalman filter double estimator designed in this paper achieve the desired results, but there are still some shortcomings.

In future research on the driving state estimation of four-wheel independent drive electric vehicles, more attention will be paid to the optimization and innovation of the algorithm. Due to the limited experimental equipment and experimental conditions, the algorithm involved has not been verified by real vehicles, and it has not been combined with advanced sensor technology, such as laser radar, millimeter-wave radar high-definition camera, and so on. In future research, we can consider the combination of these to achieve a comprehensive perception of the environment around the vehicle and its own state. In order to reduce the error caused by the model accuracy in the filtering process and make the model closer to reality, artificial intelligence technologies such as high-performance computing platforms and deep learning can be considered to build a more accurate, degree-of-freedom, and robust state estimation model. For example, a vehicle motion state estimation based on a hybrid neural network is proposed in reference [34], which realizes an accurate vehicle motion state estimation without a dynamic model. Reference [35] combines a neural network and an unscented Kalman filter to estimate the state of a multi-axle special vehicle to achieve low-cost estimation and effectively avoid the dynamic nonlinearity and uncertainty of the vehicle. The vehicle model established in this paper makes a series of assumptions, so there is still a certain gap between simulation and a real workshop. Compared with the above literature research methods, this paper is still lacking, and we should continue to learn about artificial intelligence technology in future research to achieve higher precision estimation and real-time performance.

6. Conclusions

The ongoing global scientific and technological revolution, coupled with the transformation of various industries, has significantly stimulated the trend toward electrification and intelligence in the automotive sector. This shift is driven by the need to further reduce costs associated with intelligent four-wheel drive technology while ensuring the effectiveness of active safety control systems. Additionally, it aims to enhance the stability of vehicles during high-speed travel and improve their maneuverability at low speeds. Based on the unique structure optimization and information fusion technology of four-wheel independent drive electric vehicles and considering the influence of noise on estimation accuracy in many directions, this paper designs an improved driving state estimator based on federal Kalman. The main work is summarized as follows:

The characteristics of the kinematic model and dynamic model are analyzed, and a three-degree-of-freedom nonlinear dynamic model and Dugoff tire model are established

to form the vehicle estimation model. At the same time, in order to verify the subsequent estimation algorithm based on the CarSim software (CarSim2019.0), analyze the changes in the power system of the research object, and complete the establishment of the vehicle simulation model.

In this paper, the vehicle state estimation algorithm is designed and improved using a federal Kalman filter. Considering the error accumulation and other factors of the model parameters, modifications are incorporated into the federated Kalman filter to augment the algorithm's fault tolerance. The sub-filter combines the volume Kalman filter with robust estimation theory, and the antlion optimization module is designed in the lower layer of the main filter. Based on this, the vehicle driving state estimation algorithm is designed, and the experimental conditions that are widely used in the development and verification of stability control systems are selected to verify it. Through comparison, it was found that the improved algorithm has obvious advantages in estimation precision and real-time responsiveness.

Considering the functional relationship between driving state parameters and road surface adhesion coefficient, a comprehensive joint estimation algorithm for vehicle state parameters and road surface adhesion coefficient is designed to estimate the road surface adhesion coefficient accurately, providing feedback to the driving state estimator for continuous correction, so as to consider the dynamic characteristics of the pavement, thus enhancing the adaptability of the estimation algorithm to different pavement conditions.

Author Contributions: Conceptualization, Z.C. and G.L.; methodology, Z.C., R.F. and G.L.; software, R.F., G.L. and Z.C.; validation, Z.C., G.L. and Z.Z.; formal analysis, Z.C.; investigation, Z.Z., R.F. and G.L.; resources, G.L., R.F. and Z.Z.; data curation, Z.C. and Z.Z.; writing—original draft preparation, Z.C.; writing—review and editing, Z.C. and G.L.; visualization, Z.C., G.L. and Z.Z.; supervision, G.L. and Z.Z.; project administration, G.L. and Z.Z.; funding acquisition, G.L. and Z.Z. All authors have read and agreed to the published version of the manuscript.

Funding: This research was funded by the General Program of the Natural Science Foundation of Liaoning Province in 2022 (2022-MS-376) and the Natural Science Foundation joint fund project (U22A2043).

Data Availability Statement: The original contributions presented in the study are included in the article, further inquiries can be directed to the corresponding author.

Conflicts of Interest: The authors declare no conflicts of interest.

References

1. Wang, X.B.; Han, H.; Shi, S.M. Coupling characteristics of driver pre-view time and road bend radius. *J. Jiangsu Univ.* **2022**, *43*, 249–255.
2. Liang, B.Y.; Wang, Y.P.; Liu, X. Research on crosswind stability control of high speed vehicle based on sliding mode theory. *Automot. Eng.* **2022**, *44*, 123–130.
3. Kang, C.; Lee, M.; Chung, S. Multirate lane-keeping system with kinematic vehicle model. *IEEE Trans. Veh. Lar Technol.* **2018**, *10*, 9211–9222. [CrossRef]
4. Tang, B.; Yin, Y.; Jiang, H.B. Lane tracking control of commercial vehicle based on RMPC. *J. Jiangsu Univ.* **2022**, *43*, 256–262.
5. Wiseman, Y. Autonomous Vehicles. In *Encyclopedia of Information Science and Technology*, 5th ed.; Khosrow-Pour, M., Ed.; Chapter 1; IGI Global: Hershey, PA, USA, 2020; Volume 1, pp. 1–11.
6. Liu, G.P.; Luo, Y.T. Study on the influence of Tire pressure on Automobile performance. *Guangdong Public Secur. Sci. Technol.* **2003**, *1*, 58–64.
7. Sun, X.F.; Mei, G.H.; Zhang, K.K.; Wang, Q.L.; Li, H.M. Simulation analysis of tire handling and stability based on seven-degree-of-freedom vehicle model simulation platform. *Rubber Sci. Technol.* **2023**, *21*, 583–588.
8. Liu, Y.B.; Li, S.; Chang, G.X.; Lu, F. Subjective and objective evaluation test method for tire selection. *Beijing Automob.* **2023**, *3*, 5–9.
9. Liu, K.; Wang, J.; Qu, B.J.; Wang, C.; Wei, C.L. Study on the correlation of Design factors for handling and Stability of car Tire. *Tire Ind.* **2023**, *43*, 521–524.
10. Jing, H. The influence of Automobile Tire on Automobile performance. *Tianjin Sci. Technol.* **2022**, *49*, 14–19.
11. Chen, Z.; Liu, C.Y.; Zhao, J.B.; Li, Y.H.; Liu, Y.W. A Summary of Research on handling and Stability of four-wheel Independent Drive Electric vehicle. *J. Change Inst. Technol.* **2023**, *36*, 23–27.

12. Liu, J.Q. *Research on Tire Optimization Based on Vehicle Speed Handling and Stability*; Qingdao University of Science and Technology: Qingdao, China, 2022.
13. Yao, Y.; Yan, Y.; Peng, L.; Han, D.; Wang, J.; Yin, G. Longitudinal and Lateral Coordinated Control of Distributed Drive Electric Vehicles Based on Model Predictive Control. In Proceedings of the 6th CAA International Conference on Vehicular Control and Intelligence (CVCI), Nanjing, China, 28–30 October 2022; pp. 1–6.
14. Arndt, M.; Ding, E.; Massel, T. Observer based diagnosis of roll rate sensor. In Proceedings of the American Control Conference, Boston, MA, USA, 30 June–2 July 2004; pp. 1540–1545.
15. Yang, K.; Dong, D.; Ma, C.; Tian, Z.; Chang, Y.; Wang, G. Stability control for electric vehicles with four in-wheel-motors based on sideslip angle. *World Electr. Veh. J.* **2021**, *12*, 42. [CrossRef]
16. Chu, W. *State Estimation and Coordinated Control for Distributed Electric Vehicles*; Springer: Berlin/Heidelberg, Germany, 2015.
17. Shao, X.L.; Si, H.N.; Zhang, W.D. Fuzzy wavelet neural control with improved prescribed performance for MEMS gyroscope subject to input quantization. *Fuzzy Sets Syst.* **2021**, *411*, 136–154. [CrossRef]
18. Lenzo, B.; Bucchi, F.; Sorniotti, A. On the handling performance of a vehicle with different front-to-rear wheel torque distributions. *Veh. Syst. Dyn.* **2018**, *57*, 1685–1704. [CrossRef]
19. Cheng, S.; Li, L.; Chen, J. Fusion algorithm design based on adaptive SCKF and integral correction for side-slip angle observation. *IEEE Trans. Ind. Electron.* **2018**, *65*, 5754–5763. [CrossRef]
20. Liu, W.; He, H.; Sun, F. Vehicle state estimation based on minimum model error criterion combining with extended Kalman filter Frankl. *J. Frankl. Inst.* **2016**, *353*, 834–856. [CrossRef]
21. Gustafsson, F.; Ahlqvist, S.; Forssell, U. *Sensor Fusion for Accurate Computation of Yaw Rate and Absolute Velocity*; SAE Paper 2001-01-1064; SAE International: Warrendale, PA, USA, 2001.
22. Boada, B.L.; Boadam, J.L.; Gauchia, A. Sideslip angle estimator based on ANFIS for vehicle handling and stability. *J. Mech. Sci. Technol.* **2015**, *29*, 1473–1481. [CrossRef]
23. Zhang, Q.; Liu, Z.Y.; Gu, M.Q. Vehicle sideslip angle estimation based on switched fuzzy model. In Proceedings of the 58th Conference on Decision and Control (CDC), Nice, France, 11–13 December 2019; pp. 4817–4822.
24. Zhong, H.W.; Xiao, L.; Chen, W.G.; Pu, J.L.; Liu, B. Design of four-wheel steering control algorithm for long wheelbase vehicle. *Control. Inf. Technol.* **2024**, *2*, 81–88.
25. Ji, X.; Li, G.; Fan, D.S. Study on joint estimation of vehicle state and parameters. *Comput. Simul.* **2022**, *39*, 127–134.
26. Wu, Y.F. *Estimation of Vehicle State and Road Adhesion Coefficient of Four-Wheel Independent Drive and Steering Electric Vehicle*; Jilin University: Changchun, China, 2020.
27. Chan, C.C. *Renaissance and Electric Vehicles Development*; Springer: Singapore, 2017; pp. 1–9.
28. Jin, X.J.; Yin, G.D.; Chen, N.; Chen, J.S.; Zhang, N. State observation of square root volume Kalman filter for distributed drive electric vehicles. *J. Southeast Univ.* **2016**, *46*, 992–996.
29. Xiao, F. *Research on State Estimation and Direct Yaw Moment Control of Electric Vehicle Driven by Hub Motor*; Jilin University: Changchun, China, 2016.
30. Reina, G.; Leanza, A.; Messina, A. Terrain estimation via vehicle vibration measurement and cubature Kalman filtering. *J. Vib. Control.* **2020**, *26*, 885–898. [CrossRef]
31. Wang, Y. *State and Parameter Estimation of Four-Wheel Independent Drive and Steering Electric Vehicle*; Liaoning University of Technology: Jinzhou, China, 2018.
32. Zhou, W.Q.; Qi, X.; Chen, L.; Xu, X. Vehicle state estimation based on unscented Kalman filter and genetic algorithm. *Automob. Eng.* **2019**, *41*, 198–205.
33. SkullFang. Regression Evaluation indexMSE, RMSE, MAE, R-Squared. Available online: https://blog.csdn.net/skullFang/article/details/79107127 (accessed on 25 February 2018).
34. Gao, Z.H.; Wen, W.H.; Tang, M.H.; Zhang, J.; Chen, G.Y. Vehicle Motion State estimation based on Hybrid Neural Network. *Automob. Eng.* **2022**, *44*, 1527–1536.
35. Shu, H.B.; Yu, C.Q.; Liu, Z.H.; Tang, S.J.; Chen, J.W. State estimation of Multi-axis Special vehicle based on Neural Network and unscented Kalman filter. *J. Beijing Univ. Aeronaut. Astronaut.* **2022**.